

2-P

NASA TECHNICAL
MEMORANDUM

NASA TM X-62,113

NASA TM X-62,113

Reproduced from
best available copy.



(NASA-TM-X-62113) EXPERIMENTAL SURFACE
FLOW PATTERNS AND FLOW-FIELD PHENOMENA OF A
DELTA-WING SPACE-SHUTTLE ORBITER J.W.
Cleary (NASA) Feb. 1972 51 p CSDL 20D

N72-24365

Unclas
G3/12 28207

EXPERIMENTAL SURFACE FLOW PATTERNS AND FLOW-FIELD
PHENOMENA OF A DELTA-WING SPACE-SHUTTLE ORBITER

Joseph W. Cleary

Ames Research Center
Moffett Field, California 94035

February 1972



EXPERIMENTAL SURFACE FLOW PATTERNS AND FLOW-FIELD
PHENOMENA OF A DELTA-WING SPACE-SHUTTLE ORBITER

by

Joseph W. Cleary

ABSTRACT

Composite photographs of the surface flow and shadowgraphs of the shock-wave pattern are presented that depict the hypersonic flow field of a typical delta-wing space-shuttle orbiter. Results from a wind-tunnel test in air are given in side, oblique, and projected plan views for angles of attack from 0° to 60° . The tests were conducted at a Mach number of 7.4 and for Reynolds numbers based on body length of 6×10^6 and 9×10^6 . The composites demonstrate the interrelation of the intersecting bow and wing leading-edge waves with the surface flow for angles of attack for which: (1) the leading-edge wave is attached, and (2) the leading-edge wave is detached.

EXPERIMENTAL SURFACE FLOW PATTERNS AND FLOW-FIELD PHENOMENA OF A DELTA-WING SPACE-SHUTTLE ORBITER

by

Joseph W. Cleary

INTRODUCTION

Reusable space-shuttle vehicles that can terminate an earth orbital mission with a conventional airplane-type landing are currently evolving as a device for transporting personnel and equipment to and from earth orbit. The performance of these vehicles is dependent in part on reliable estimates of heating during the entry phase of the trajectory. An analysis of heating for the entry mode requires information on the flow field in order that an accurate estimate of flow conditions at the edge of the boundary layer can be made. Moreover, information on the flow-field can be helpful as a guide in the selection of the size and disposition of the various components of the vehicle such as the canopy, wing, tail, and control surfaces.

Considerable information of the flow field can be obtained from shadowgraphs of the shock-wave pattern. In addition, surface flow visualization by the oil-streak method gives visual evidence of the complexities of the surface flow that can be associated with the shock-wave pattern. The purpose of the present investigation is to present, in support of the orbiter heating analysis and preliminary design, composites of the surface flow and shock-wave pattern of a typical delta-wing vehicle that depict the interrelation of these flow field boundaries. The investigation was conducted on a 0.0075-scale model of the 134 full-scale orbiter concept proposed by North American Rockwell Corporation for the high cross-range mission. The model has a centerline vertical tail with 20° flared surfaces. The stability and control characteristics of this configuration are given in references 1 and 2 and shadowgraphs of the flow are given in reference 3. Measurements of heating on a twin-tailed version of this configuration are presented in reference 4 and summarized in reference 5. Surface flow patterns of a related twin-tailed configuration are given in reference 6 but for lower Reynolds numbers than the present test results. The results compiled herein present, in more complete form, preliminary surface flow results presented in reference 7.

The investigation was conducted in a hypersonic wind tunnel at a Mach number of 7.4 and for Reynolds numbers based on body length of 6×10^6 and 9×10^6 . Composite photographs of the flow are depicted in side, oblique, and plan views for angles of attack from 0° to 60°. In addition, results are given to demonstrate the flow asymmetry of the sideslip mode for a sideslip angle of -10° at an angle of attack of 15°.

The symbols used in presenting the test results are defined as follows:

L	body length
M_{∞}	free-stream Mach number
$Re_{\infty L}$	free-stream Reynolds number based on model length
x	body axial coordinate
α	angle of attack
β	angle of sideslip
ϕ	roll angle of the sting with respect to the free-stream velocity

TESTS AND EQUIPMENT

Model

A three-view sketch, photographs of the model, and other information pertinent to the test are presented in figure 1. Dimensional details of model are given in Table I. The model was fabricated from a brass casting. The mold for the cast was formed from the 0.00763-scale model used in the investigation of reference 1. Because of shrinkage of the cooled casting and finishing and polishing of the model, the final dimensions of the model were about 1.5-percent less than those of the original model and yielded a model scale of 0.0075. The vertical tail with 20° flared surfaces aft of the 0.6 chord line was made of steel and attached to the body in a slot (see figures 1(b) and (c)). The model was supported by a one-inch diameter dummy balance housed within the model with its axis parallel to the model reference axis.

Facility and Tests

The investigation was conducted in the Ames 3.5-foot hypersonic wind tunnel during April, 1971. The tests were made in air at a Mach number of 7.38 and for free-stream Reynolds numbers based on body length 6.0×10^6 and 9.0×10^6 . The total temperature of the reservoir was maintained within the range from about 1200°R to 1300°R.

For the test results that are depicted by shadowgraphs, the model was mounted on the tunnel centerline sting and strut support. For tests in pitch, the sting support was maintained at 0° incidence and the angle of attack of the model was varied by installing incidence brackets of 0°, 15°, 30°, 45°, and 60° between the model and the sting. The model was rolled about the sting axis (effectively the free-stream velocity) to the desired angle ϕ that was required to give side, oblique, and projected plan

views of the flow. The upright model position (wings horizontal) is assumed for $\phi = 0^\circ$ and, as shown in figure 1(d), left wing down is selected to define a positive angle for roll. With the wings vertical, $\phi = 90^\circ$, the model was sideslipped by pitching the sting and strut support to the desired sideslip angle.

The model could be translated vertically by moving the strut support, and before each run the model was prepositioned in this manner near tunnel centerline and in view of a photographic plate mounted adjacent to a side-wall window. Parallel light was reflected through the test section to cast a full-scale shadowgraph of the flow over the model on the photographic plate.

For the surface-flow visualization tests, the model was mounted on the quick-insert support strut which enters the tunnel after flow is established and withdraws after a prescribed time interval. The model was supported in the same manner and for the same angles of attack as that for shadowgraphs except the wing was maintained vertical $\phi = 90^\circ$. Before each run the black-lacquer-painted model was coated with a thin film of a mixture of oil and titanium oxide. The coated model was exposed to the tunnel flow for about 3 seconds and then retracted. Subsequent to the run, the model with the surface flow imposed was photographed at essentially the same orientation as that for the shadowgraph of the flow that was projected on the tunnel window photographic plate. Subsequently, the surface flow was superimposed on the shadowgraph of the shock-wave pattern to give a photographic composite of the flow. Untouched shadowgraphs of the flow are presented in reference 3.

Before each run, the model was repainted and smoothly finished. However, because of impingement of fine dust particles from the pebble-bed heater on the model during the run, the model became slightly abraded at the termination of the run. The effects of this abrasion on the nature of the boundary layer is not known, but for the hypersonic test conditions, the effects are believed not to be significant.

RESULTS AND DISCUSSION

Effects of Angle of Attack

Composite photographs of the surface streamlines and shadowgraphs of the shock-wave pattern that depict the effects of angle of attack on the flow are presented in figures 2 to 6. Results are given for angles of attack from 0° to 60° in increments of 15° . For each angle of attack, the figures display the flow sequentially for 5 roll angles, ϕ , from -90° to 90° in increments of 45° . This range of roll angles encompasses, in addition to the side view, the projected plan and oblique views for both windward and leeward surfaces. The shadowgraphs of the shock-wave patterns on which the surface flows are superimposed were presented initially in reference 3. The shaded background of the figures is not relevant to the flow since it was incurred in the shadowgraphs from a window imperfection.

It is expedient to discuss initially the flows for which the wing leading-edge wave is attached and then consider flows for which the wing leading-edge wave is detached. Aside from the effects of airfoil leading-edge bluntness, the leading-edge wave is, of course, attached at low angles of attack. With increasing angle of attack, the leading-edge wave detaches in a manner similar to that for a sharp leading-edge conical flow. While the angle of attack for wave detachment is not known, it is apparent from differences in the shock-wave pattern at the wing-tip apex, as shown in figures 3(a) and 4(a), that detachment occurred between 15° and 30° angle of attack.

Leading-edge wave attached.- The flow over the model with the leading-edge wave attached is depicted in figures 2 and 3 for $\alpha = 0^\circ$ and 15° respectively. At $\alpha = 0^\circ$, the flow of the white oil mixture over the windward surface (figures 2(a) and (b)) appears to terminate about where the slope of the local surface parallels the free-stream flow. It is believed this termination of the oil streaks results from low viscous shear below some threshold level that is dependent on the viscosity of the oil. It appears doubtful that the flow is separated in the sense that a dividing streamline leaves the surface and divides the flow from the separated reverse flow as can occur, e.g. on the lee side (see figure 3(e)).

For $\alpha = 0^\circ$, figure 2(c) shows, in side view, that because of body camber the flow is from the upper surface of the nose towards the lower surface. Further aft on the body, a faint stagnation line can be seen that forms below the canopy at about the maximum width of the body. This stagnation line merges with the fillet and wing leading-edge stagnation line and thereby demarcates the windward flow from the lee-side flow. Because for $\alpha = 0^\circ$ the canopy is unshielded from the free stream, the lee-side flow appears dominated by interference effects of the canopy. Figure 2(c) shows that the bow wave intersects and merges with the canopy wave. A discontinuity can be seen in the flow field downstream of the intersection.

Since both waves are of the same family, this discontinuity may be a slip surface or vortex sheet that results from the intersection of the waves. This discontinuity intersects the vertical-tail leading-edge wave at about midspan and appears to have only a small effect on the leading-edge wave and on the flow over the 20° flared vertical tail.

The canopy wave is attached to the apex of the canopy and it intersects the body to form a curved separation line ahead of the canopy windshield. This separation line merges with dark streaks below the canopy on the sides of the body where the canopy wave intersects the body surface (see figure 2(d)). Since the canopy wave is not visible in the plan view of figure 2(e), it is apparent that the bow wave and canopy wave intersect along a curve in space. The oblique view given in figure 2(d) has about the proper perspective to, in essence, show a segment of the curve of wave intersection.

Figure 2(e) shows that the bow wave intersects the wing leading-edge wave and crosses the wing at about midsemispan. For $\alpha = 0^\circ$, the visible apparent intersection of the waves and the true intersection in the plane of the wing are essentially coincident. It can be seen that outboard of where the bow wave crosses, the flow has passed through only the leading-edge wave and the surface flow is essentially attached. However, the attached flow over this outboard surface of the wing may result in part from the geometrical twist (5° washout) of the wing.

The accumulation of the oil in chordwise streaks on the wing that are shown in figure 2(e) is believed due to vortices that form in a three-dimensional boundary layer. Observations on three-dimensional boundary layers given in reference 8 indicate that the axes of the vortices tend to align with the direction of the flow at the boundary-layer edge and moreover, the vortices are precursors to the development of turbulent flow.

At $\alpha = 15^\circ$, figures 3(a) and (b) show that, because of crossflow, the surface streamlines diverge significantly on the windward surface of the body forward of the wing. On the other hand, aft of the fillet the flow over the body is essentially two dimensional (parallel streamlines) except for slight convergence where the body boattails as the flow approaches the base. Furthermore, it is apparent from figures 3(a) and (b) that the leading-edge stagnation line of each wing panel is a streamline originating near the centerline that essentially divides the flow streaming to the leeward side from that on the windward side. Since the wing leading-edge wave is attached for this angle of attack, the stagnation line lies along the blunt leading edge of the wing and close to the geometrical leading edge. Another streamline nearby, that originates nearer the centerline, terminates on the exposed root of the wing at the trailing edge to enclose, together with the stagnation line, a highly divergent flow over the wing

panel. Figure 3(a) and an enlargement of the wing panel given in figure 3(f) show that the streamline divergence is greatest just aft of the leading-edge stagnation line and the exposure of the black-painted surface of the wing in this region results from the attendant greater viscous shear.

The contrasting shade of darkness (figure 3(f)) is in qualitative agreement with the higher measured heating rates near the leading edge that are observed in reference 5. Furthermore, the heating rates presented in reference 5 indicate that transition to turbulent flow occurred on the body centerline at $X/L \sim .55$ for about the same test conditions as the present investigation. In addition, evidence is given in reference 5 that suggests the flow was also turbulent over the aft region of the wing. In the present results, it is believed the appearance of Mach waves in the flow field adjacent to the body boattail is associated with these observations of turbulent flow. These Mach waves are faintly visible in the side view of figure 3(c) for $\alpha = 15^\circ$ and are more clearly visible for higher angles of attack to be presented later.

Figure 3(f) does not show clearcut evidence of the interaction of the intersecting bow and wing leading-edge waves with the flow over the windward surface as did the oil-flow photographs of a straight-wing orbiter model presented in references 9 and 10. However, for the present case of the delta wing (figure 3(f)) there are subtle differences in the appearance of the streamlines of the inboard region of the wing panel when compared with those outboard that are believed associated with interaction of the intersecting waves. Moreover, the greater chordwise extent of the exposed black surface for the inboard region may be an indication of interaction and this is in agreement with observations of heating given in reference 11.

Figures 3(c), (d), and (e) indicate that for $\alpha = 15^\circ$, the flow over the leeward side is probably separated for a considerable extent of the body and wing surface. Aft of the apparently separated flow over the nose, a faint reattachment line can be seen on the centerline and this detail is shown more clearly by an enlargement of the view given in figure 3(g). This reattachment line is believed to result from a pair of body vortices that occur in the separated flow over the nose. References 12 and 13 demonstrate that body vortices are Reynolds number dependent and can significantly influence the distribution of lee-side heating.

Although at $\alpha = 15^\circ$ the vertical tail is shielded by the body, figure 3(c) shows that a complex flow pattern is imposed on the tail by the non-uniform lee-side flow. An enlargement of this flow pattern is given in figure 3(h). Pitot surveys of the flow field given in reference 7 indicate the flow over the outboard span of the tail is supersonic while nearer the root, the flow is subsonic and separated. Over the outboard span,

figure 3(h) shows a line of flow separation forward of the hingeline that is attributed to shock induced separation in the locally supersonic flow. A dividing streamline that crosses the tail near midspan denotes the approximate edge of the supersonic flow.

The interaction of the intersecting bow and wing leading-edge waves with the lee-side flow over the wing is depicted in figure 3(e) and in greater detail, by an enlargement of the surface flow given in figure 3(i). While it is apparent that the interaction for swept delta wings is a complex phenomena, it is believed to be fundamentally similar to that presented for a straight wing in references 9 and 10. Figures 3(e) and (i) show that there is a separation line just outboard of where the bow wave crosses the wing. Adjacent to the separation line, a faint reattachment line can be seen in the chordwise direction that extends to the trailing edge. The flow inboard of the interaction has traversed two oblique waves and figure 3(i) shows that the streamlines curve inboard from the leading edge. Outboard of the interaction, the flow has passed through one oblique wave and the surface streamlines have significantly less curvature than the inboard flow. Figure 3(i) shows that the prevailing direction of the surface streamlines is inboard towards the body. The body presents an obstacle to this inboard flow and the attached flow over the fillet separates along a line adjacent to the wing root.

Leading-edge wave detached.- The flow over the model with the leading-edge wave detached is presented in figures 4, 5, and 6 for angles of attack of 30° , 45° , and 60° respectively. Figures 4, 5, and 6 indicate that for the detached wave case there are no significant visible effects of wave interaction with the flow over the windward surface of the wing. In addition, it can be seen that with increasing angle of attack, the leading-edge stagnation line moves off of the airfoil nose and aft on the windward surface except near the wing-tip apex through which this dividing streamline passes. For $\alpha = 30^\circ$ and 45° , the flow over the windward surface of the wing has an unusual and contrasting appearance when compared with the whiter appearance of the body. The somewhat darker appearance of the wing panels is attributed in part to a substantial divergence of the flow. In addition, the fillet-wing-body juncture presents a discontinuity in curvature to the flow locally that can influence the surface pressure and the associated viscous shear. (See cross section of the juncture depicted in figure 1(a).)

Heating measurements (reference 5) demonstrate that for essentially the same test conditions, transition from laminar flow to turbulent flow occurred on the windward centerline at $X/L \sim .5$ for $\alpha = 30^\circ$. The appearance of flow-field Mach waves for these conditions in present results is believed associated with this observation of turbulent flow. These Mach waves are visible within the aft region of the body flow field in figure 4(c) for $\alpha = 30^\circ$ and likewise, in figure 5(c) for $\alpha = 45^\circ$.

For $\alpha = 30^\circ$ and to lesser extent for $\alpha = 45^\circ$, the Mach waves appear more concentrated aft and beneath the wing than ahead of the wing. Since for $\alpha = 30^\circ$ transition occurs on the body ahead of the exposed wing root, it is possible this concentration of waves results from the lateral spreading of the turbulent flow over the wing panels.

For $\alpha = 45^\circ$, figure 5(a) shows what appears to be a turbulent wedge on centerline that is initiated by a slight depression from a filled hole at about $X/L = .5$. The Reynolds number for this angle of attack is less than that for $\alpha = 30^\circ$ and natural transition without the depression might be further aft. While the implication from the occurrence of the turbulent wedge is that the flow was laminar or transitional at the depression, it is not possible from the surface flow alone to ascertain where natural transition occurred.

At an angle of attack of 60° , figure 6(a) shows that the greater heating and viscous shear that occurred compared to that at a lower angle of attack completely eroded the surface oil film and blistered the painted surface. Nevertheless, the streaks ingrained in the surface provide a fair indication of the streamline direction. The anomalous appearance of the bow wave adjacent to the nose resulted from the unavoidable projection of the nose into the tunnel wall boundary layer; however, this did not affect the surface flow since the model had a different orientation for these tests. For this angle of attack, Mach waves are not visible in the side view of the flow (figure 6(d)) as was the case at lower angles of attack. Measurements of the shock-wave angle just aft of the wave inflection indicate that the flow is essentially subsonic beneath the wing. Just forward of the wave inflection, the flow is supersonic behind the wave but, assuming conical-flow compression from the shock to the body (reference 14), the flow is estimated to be subsonic on the body. It is believed the essentially subsonic flow at the surface precludes the appearance of Mach waves if the flow were turbulent.

On the lee side, figures 4(e), 5(e), and 6(e) demonstrate that the flow over the wing separates nearer the leading edge with increasing angle of attack. Furthermore, for an angle of attack of 60° (figure 6(e)) the separation line is essentially on the blunt leading edge of the airfoil. Figures 4(e), 5(e), and 6(e) show that for the angle of attack range from 30° to 60° (for which the leading-edge wave is detached) the lee-side surface flow is essentially free of the effects of wave interaction. This is in sharp contrast to that for the aforementioned attached wave case (see figure 3(e)). However, since detachment occurs smoothly with increasing angle of attack, it should not be construed that significant effects of lee-side interaction are necessarily limited to flows with an attached wave.

Effects of Sideslip on the Flow

Projected plan views of the flow are given in figure 7 to show the effects of flow asymmetry for a sideslip angle of -10° and an angle of attack of 15° . From the wave pattern at the wing tips, it is apparent that the leading-edge wave of the forward wing panel is attached while that for the rearward panel is detached. Figure 7(a) shows that on the windward surface, the leading-edge stagnation line of the rearward wing panel, similar to that of the forward panel, originates near the nose on the upstream side of the body. The bow wave intersects the forward wing panel leading-edge wave near the root. On the other hand, the intersection of the bow wave with the wave from the rearward wing panel appears outside the wing tip. It is apparent in figure 7(a) from the darker and eroded appearance of the upstream side of the body and wing, that significantly greater viscous shear was incurred than on the downstream side.

On the lee side, figure 7(b) shows that the flow is attached to a greater extent on the upstream surface of the body and on the forward wing surface than on the downstream side. Furthermore, the effects of wave interaction with the surface flow over the forward wing appear nearer the root than that without sideslip. On the other hand, the surface flow on the rearward wing panel resembles that without sideslip with a detached wave but at a greater angle of attack.

CONCLUDING REMARKS

Composite photographs of the surface flow and shock-wave patterns are presented that depict the hypersonic flow field of a typical delta-wing space-shuttle orbiter. Results from wind-tunnel tests of a 0.0075-scale model are given for a Mach number of 7.4 and Reynolds numbers based on body length of 6×10^6 and 9×10^6 . The phenomenon of the interaction of intersecting bow and wing leading-edge waves with the surface flow over the wing is shown for ranges of angles of attack for which the wing leading-edge wave is attached and detached from the leading edge. The results indicate that on the windward surface of a highly swept delta wing, interaction exerts a weak influence on the surface streamlines for the Reynolds numbers of the test.

The photographs depict the pattern of flow separation on the lee side of the body and the wing for angles of attack up to 60° . On the lee side the interaction phenomenon displays its most significant influence on the surface flow of the wing at low angles of attack $\alpha \lesssim 30^\circ$ with the leading-edge wave attached. At high angles of attack $\alpha \gtrsim 30^\circ$ with the leading-edge wave detached, the lee-side surface flow appears essentially free of

the effects of interaction. It is shown that sideslip accentuates interaction effects on the forward wing panel and relieves these effects on the rearward wing panel.

REFERENCES

1. Cleary, Joseph W.: Hypersonic Stability and Control Characteristics of a Delta-Wing Space Shuttle Orbiter. NASA TM X-62,067, December 28, 1970.
2. Malcolm Gerald N.: Aerodynamic Characteristics of a Space Shuttle Delta-Wing Orbiter at Mach Numbers from 0.25 to 2.0. NASA TM X-62,044, June 1971.
3. Cleary, Joseph W.: Hypersonic Shock-Wave Phenomena of a Delta-Wing Space Shuttle Orbiter. NASA TM X-62,076, October 28, 1971.
4. Lockman, William K.; and DeRose, Charles E.: Aerodynamic Heating of a Space Shuttle Delta-Wing Orbiter. NASA TM X-62,057, August 11, 1971.
5. Marvin, J. G.; Seegmiller, H. L.; Lockman, W. K.; Mateer, G. G.; Pappas, C. C.; and DeRose, C. E.: Surface Flow Patterns and Aerodynamic Heating on Space Shuttle Vehicles. Paper No. 71-594, AIAA, June 1971.
6. Seegmiller, H. Lee: Surface-Flow Visualization Investigation of a Delta Wing Shuttle Configuration at a Mach Number of 7.4 and Several Reynolds Numbers. NASA TM X-62,036, June 2, 1970.
7. Cleary, Joseph W.: Lee Side Flow Phenomena on Space Shuttle Configurations at Hypersonic Speeds. Part I: Flow Separation and Flow Field Viscous Phenomena of a Delta Wing Shuttle Orbiter Configuration. NASA TM X-2507, Vol. 2, February 1972, NASA Aerothermodynamics Technology Conference, Dec. 1971.
8. Gregory, N.; Stuart, J. T.; and Walker, W. S.: On the Stability of Three-Dimensional Boundary Layers with Application to the Flow Due to a Rotating Disk. Phil. Trans. Roy. Soc. (London), Ser. A., vol. 248, no. 943, July 1955, pp. 155-199.
9. Seegmiller, H. Lee: Shock Interference Heating and Density-Ratio Effects. Part I: Flow Field Visualization, Thermocouple Measurements, and Analysis. NASA TM X-2272, NASA Space Shuttle Technology Conference, vol. I, April 1971.
10. Hunt, James L. and Creel, Theodore R., Jr.: Shock Interference Heating and Density-Ratio Effects. Part II: Hypersonic Density-Ratio Effects. NASA TM X-2272, NASA Space Shuttle Technology Conference, vol. I, April 1971.

11. Compton, D. L.: Convective Heating Measurements by Means of an Infrared Camera. NASA TM X-2507, vol 2, February 1972. NASA Space Shuttle Aerothermodynamic Technology Conference, Dec. 1971.
12. Hefner, Jerry N. and Whitehead, Allen H., Jr.: Lee-Side Heating Investigations. Part I: Experimental Lee-Side Heating Studies on a Delta-Wing Orbiter. NASA TM X-2272, NASA Space Shuttle Technology Conference, vol. I, April 1971.
13. Maise, George: Lee-Side Heating Investigations. Part II: Lee-Side Heating Investigations of Simple Body-Like Configurations. NASA TM X-2272, NASA Space Shuttle Technology Conference, Vol I, April 1971.
14. Cleary, Joseph W.: Approximation for Distribution of Flow Properties in the Angle of Attack Plane of Conical Flows. NASA TN D-5951, August 1970.

TABLE I
MODEL DIMENSIONS

Body

Length, inches	15.9
Maximum width, inches	3.49
Maximum depth, inches	2.04
Fineness ratio	6.18
Maximum cross-sectional area, square inches	5.15

Complete Delta Wing

Planform area, square inches	49.3
Span, inches	10.7
Aspect ratio	2.31
Rate of taper	1.73
Taper ratio	0.0
Dihedral angle, degrees	7.0
Root incidence angle, degrees	0.0
Aerodynamic twist, degrees	-5.0
Sweep-back angles	
Leading edge, degrees	60.0
Trailing edge, degrees	0.0
0.25 Element line, degrees	52.2
Chords	
Root (wing station 0.0 inches), inches	9.24
Tip, inches	0.0
Mean aerodynamic chord, inches	6.16
Airfoil Section	
Root (wing station 1.80 inches)	NACA 0009-64
Tip (wing station 4.06 inches)	NACA 0012-64

Elevon, One Panel

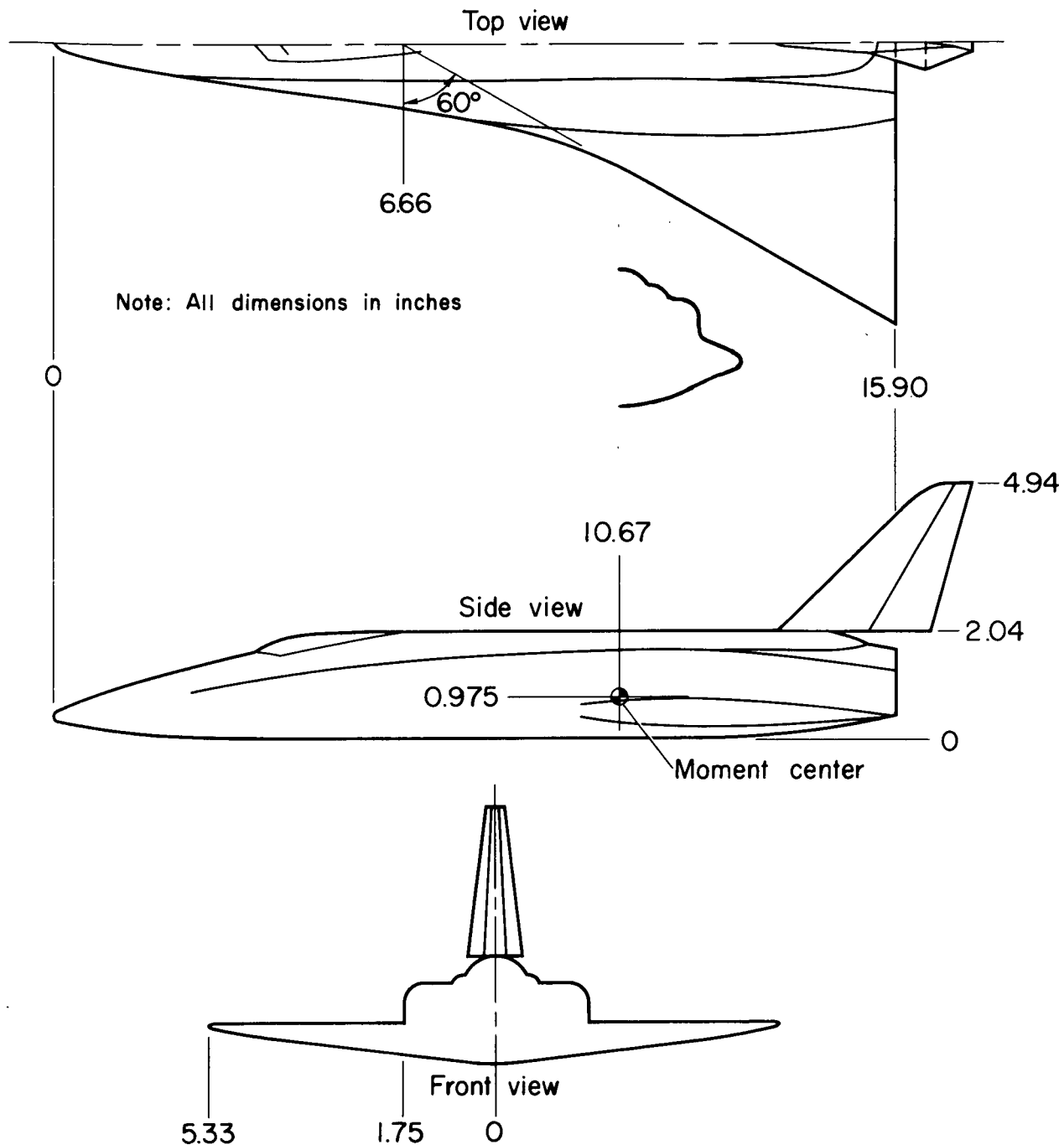
Planform area, square inches	4.00
Span, inches	4.07
Inboard chord, inches	1.00
Outboard chord, inches	1.00

TABLE I con't

Sweepback angles	
Leading edge, degrees	0.0
Trailing edge, degrees	0.0
Hingeline, degrees	0.0

Centerline Vertical Tail

Planform area, square inches	5.60
Span, inches	2.90
Aspect ratio	1.48
Rate of taper	0.72
Taper ratio	.31
Sweep-back angles	
Leading edge, degrees	45.0
Trailing edge, degrees	15.8
0.25 Element line, degrees	39.4
Chords	
Root, inches	2.98
Tip, inches	0.91
Mean aerodynamic chord, inches	2.13
Airfoil section: Root and tip sections are 5° semi-vertex blunted wedges with 20° flared edges aft of 0.6 chord.	



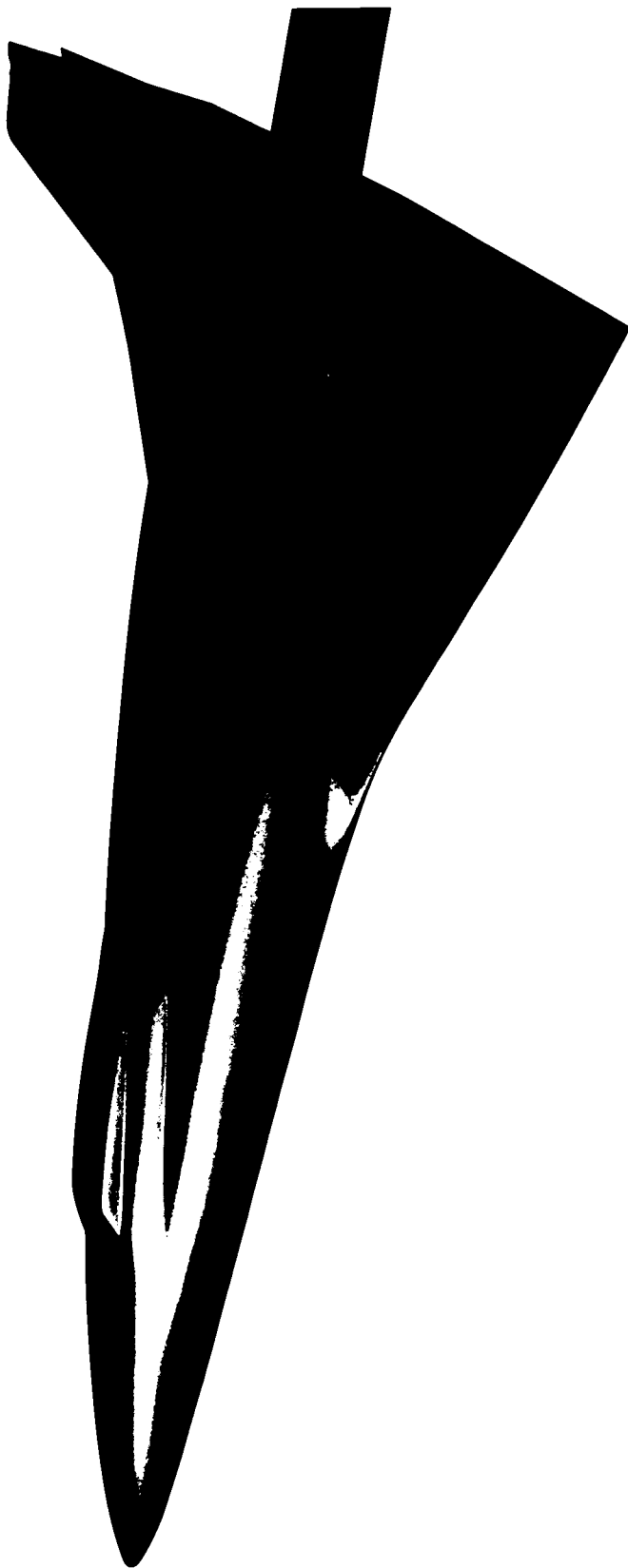
(a) Sketch of the model.

Figure 1.- Model dimensions, photographs and definitions.



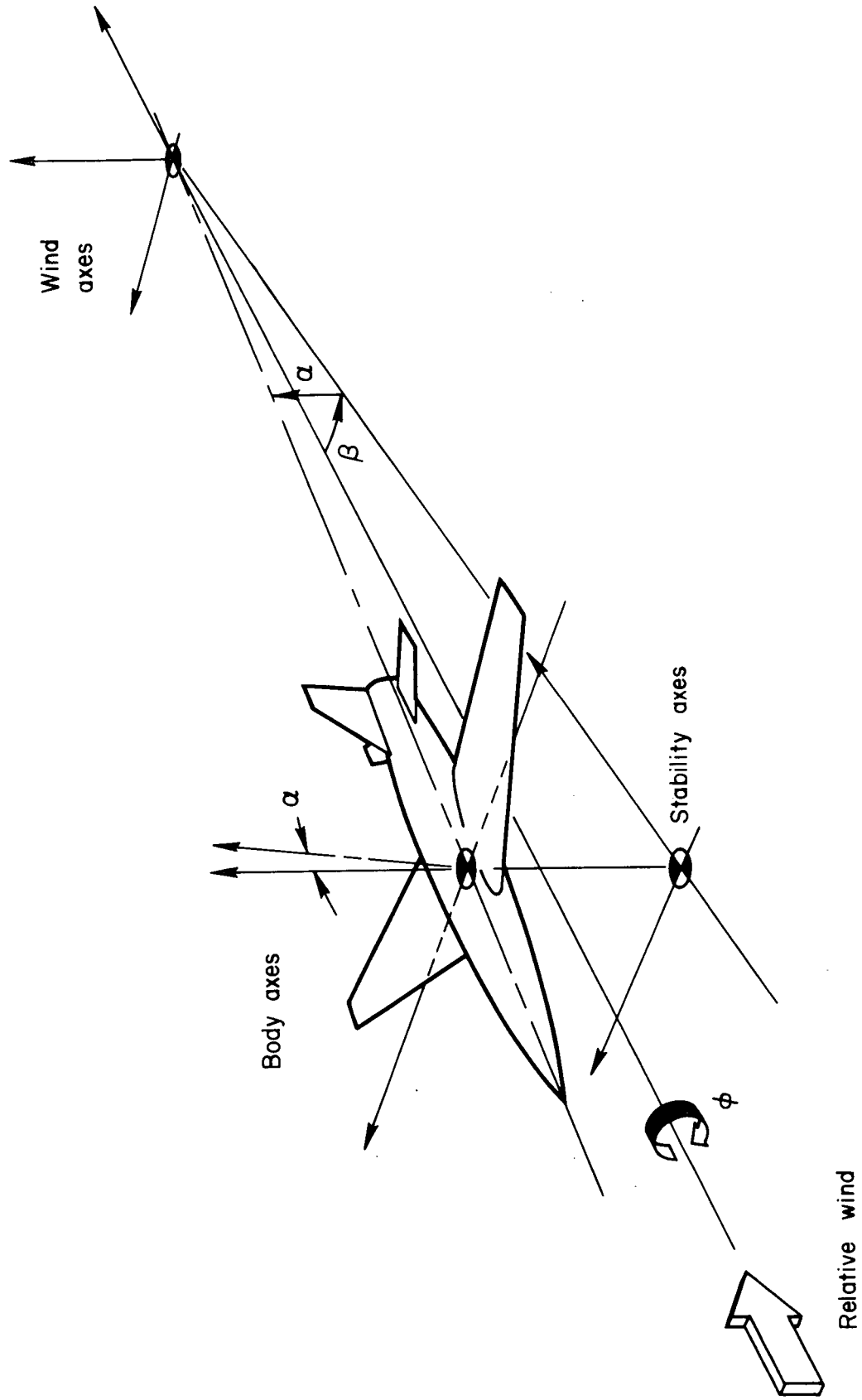
(b) Three-quarter front view of the model.

Figure 1.- Continued.



(c) Three-quarter rear view of the model.

Figure 1.- Continued.



(d) Model orientation.

Figure 1.- Concluded.



(a) Plan view of the windward surface, $\phi = -90^\circ$.

Figure 2.- Flow over the model at an angle of attack of 0° .

$\beta = 0^\circ$, $M_\infty = 7.4$, $Re_\infty = 9.0 \times 10^6$.



(b) Oblique view of the windward surface, $\phi = -45^\circ$.

Figure 2.- Continued.



(c) Side view, $\phi = 0^\circ$.

Figure 2.- Continued.



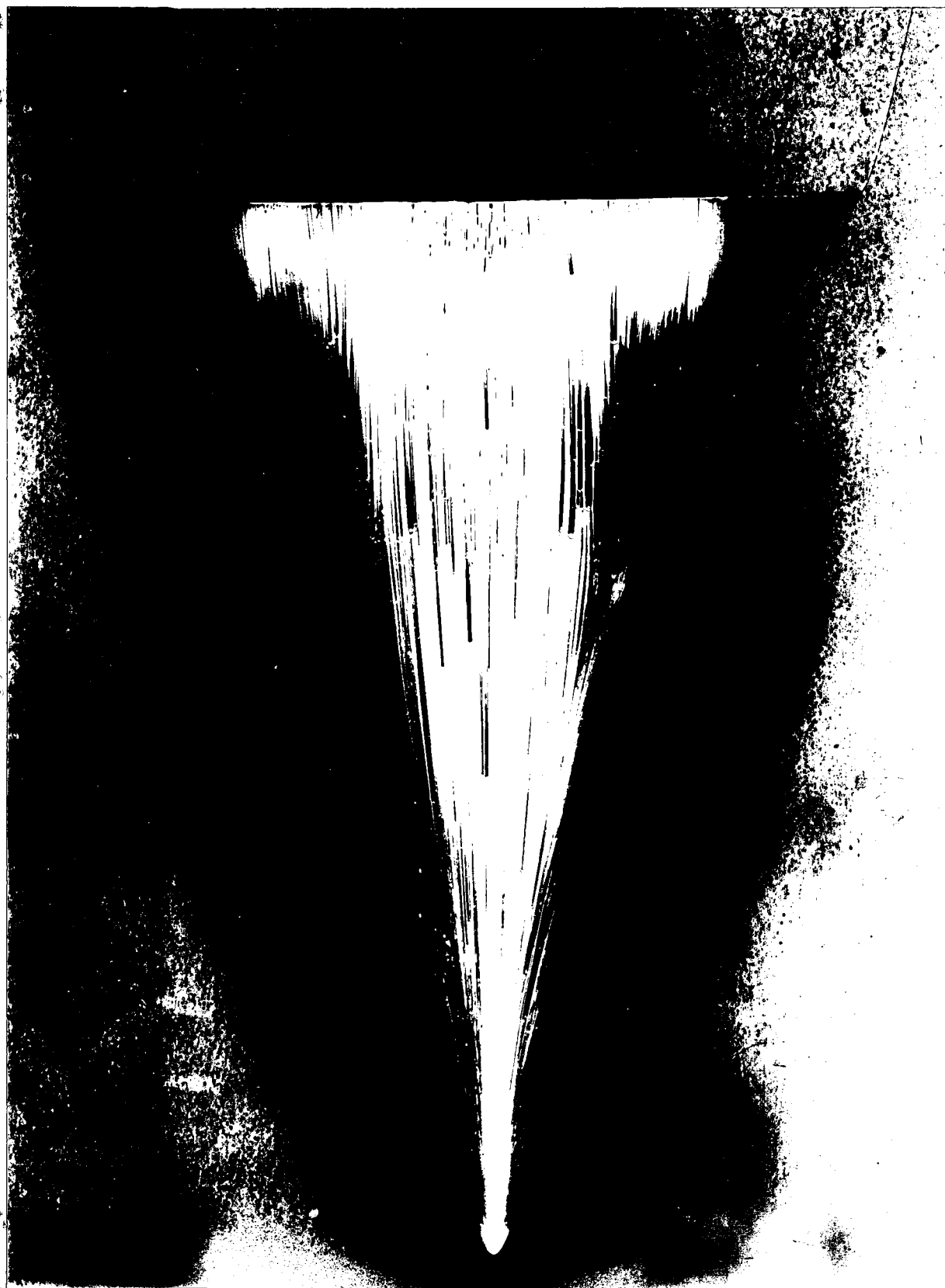
(d) oblique view of the leeward surface, $\phi = 45^\circ$.

Figure 2.- Continued.



(e) Plan view of the leeward surface, $\phi = 90^\circ$.

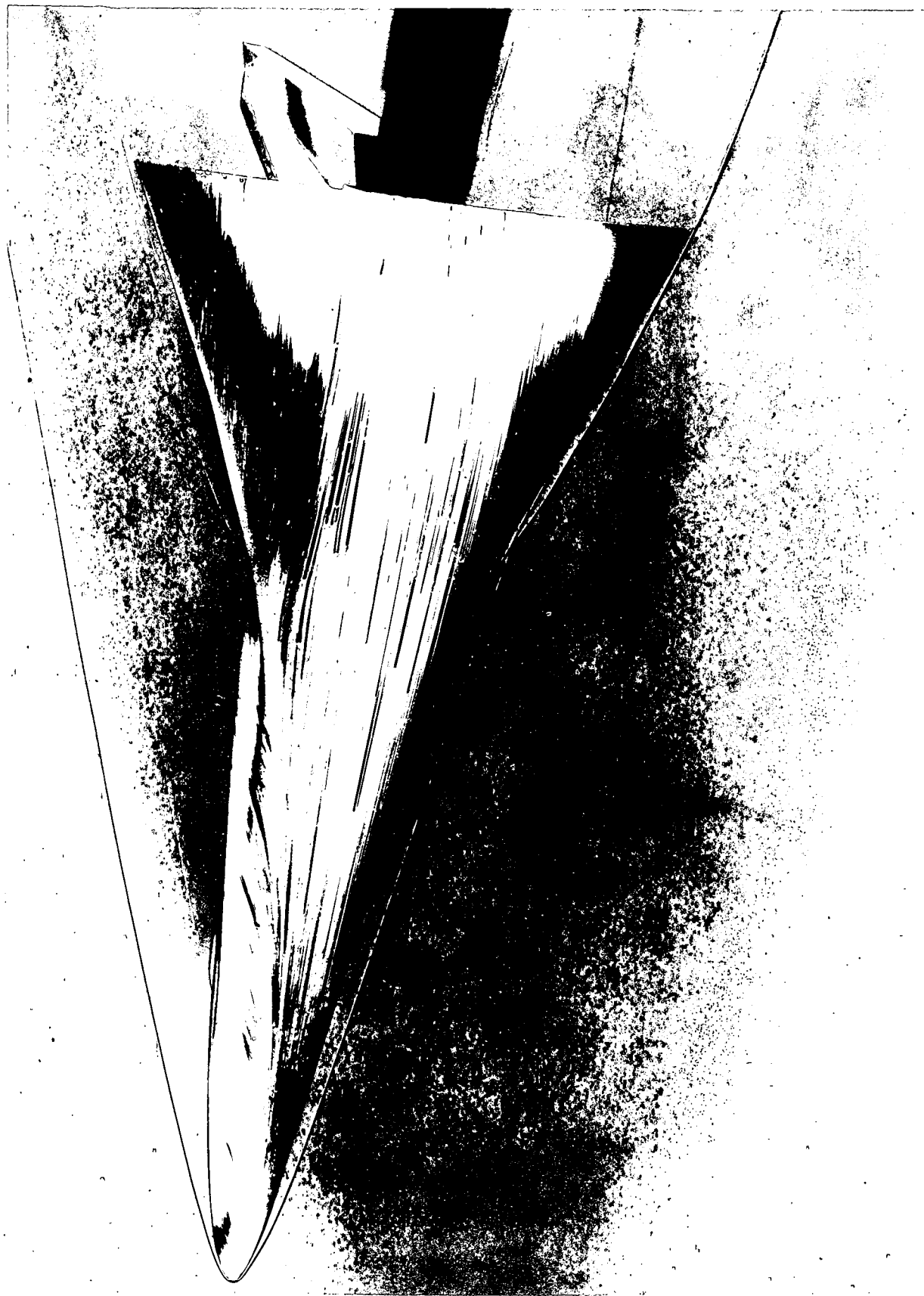
Figure 2.- Concluded.



(a) Plan view of the windward surface, $\phi = -90^\circ$.

Figure 3.- Flow over the model at an angle of attack of 15° .

$\beta = 0^\circ$, $M_{\infty} = 7.4$, $Re_{\infty} = 9.0 \times 10^6$.



(b) Oblique view of the windward surface, $\phi = -90^\circ$.

Figure 3.- Continued.



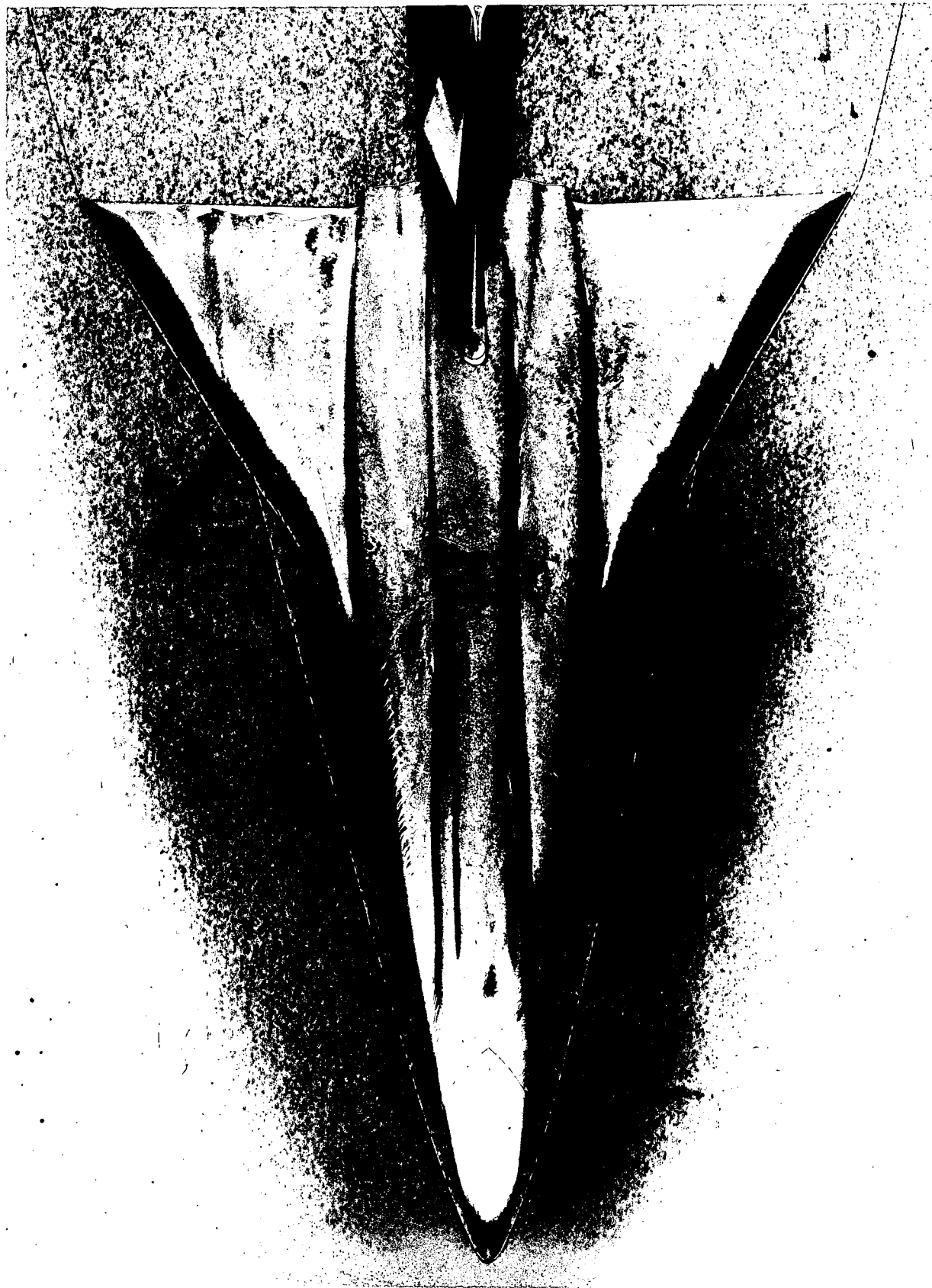
(c) Side view, $\phi = 0^\circ$.

Figure 3.- Continued.




(d) Oblique view of the leeward surface, $\phi = 45^\circ$.

Figure 3.- Continued.



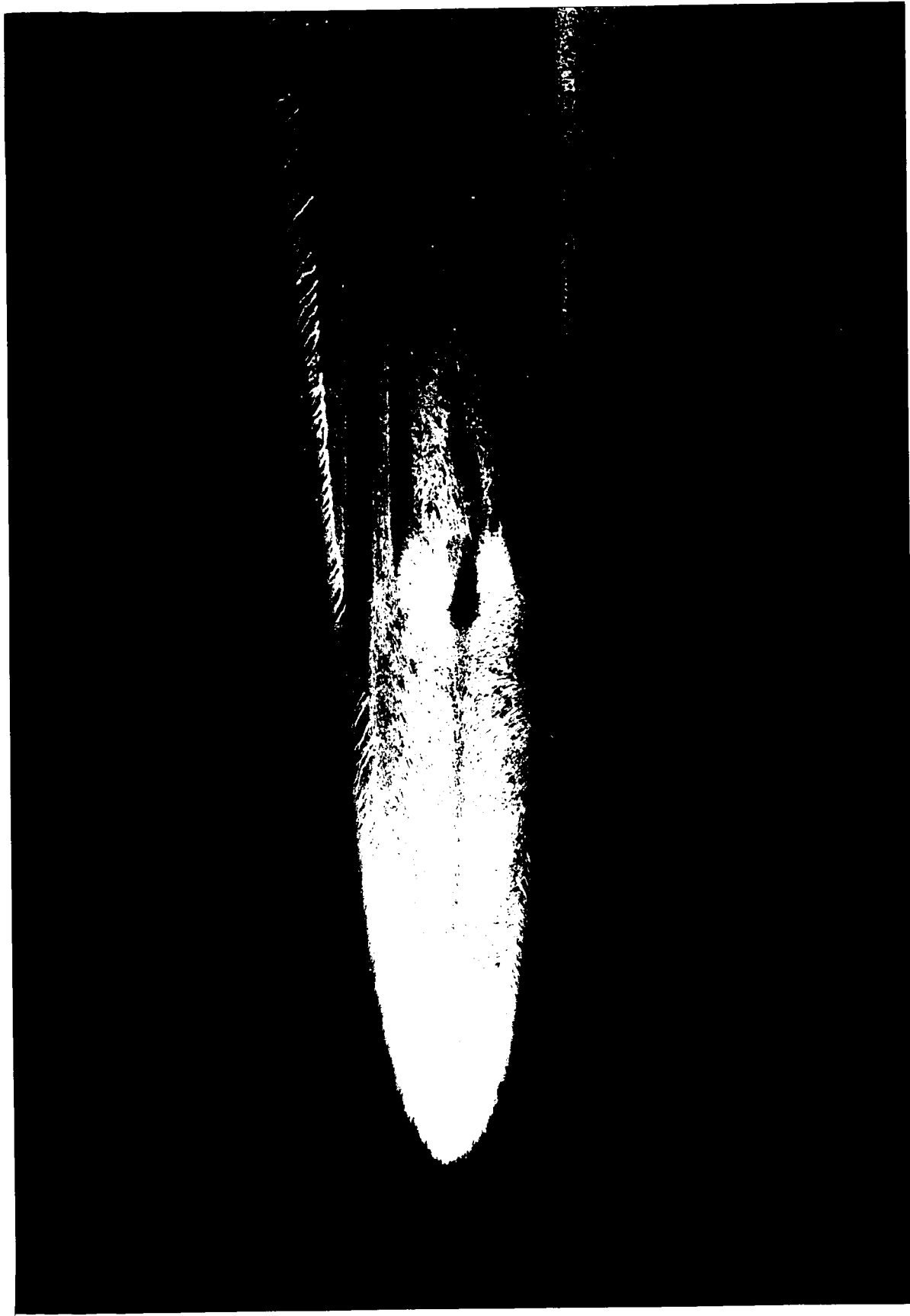
(e) Plan view of the leeward surface, $\phi = 90^\circ$.

Figure 3.- Continued.



(f) Plan view of the wing panel on the
windward side, $\phi = -90^\circ$.

Figure 3.- Continued.



(g) Plan view of the nose on the lee
side, $\phi = 90^\circ$.

Figure 3.- Continued.



(h) Side view of the vertical tail, $\phi = 0^\circ$.

Figure 3.- Continued.



(i) Plan view of the wing panel on the
lee side, $\phi = 90^\circ$.

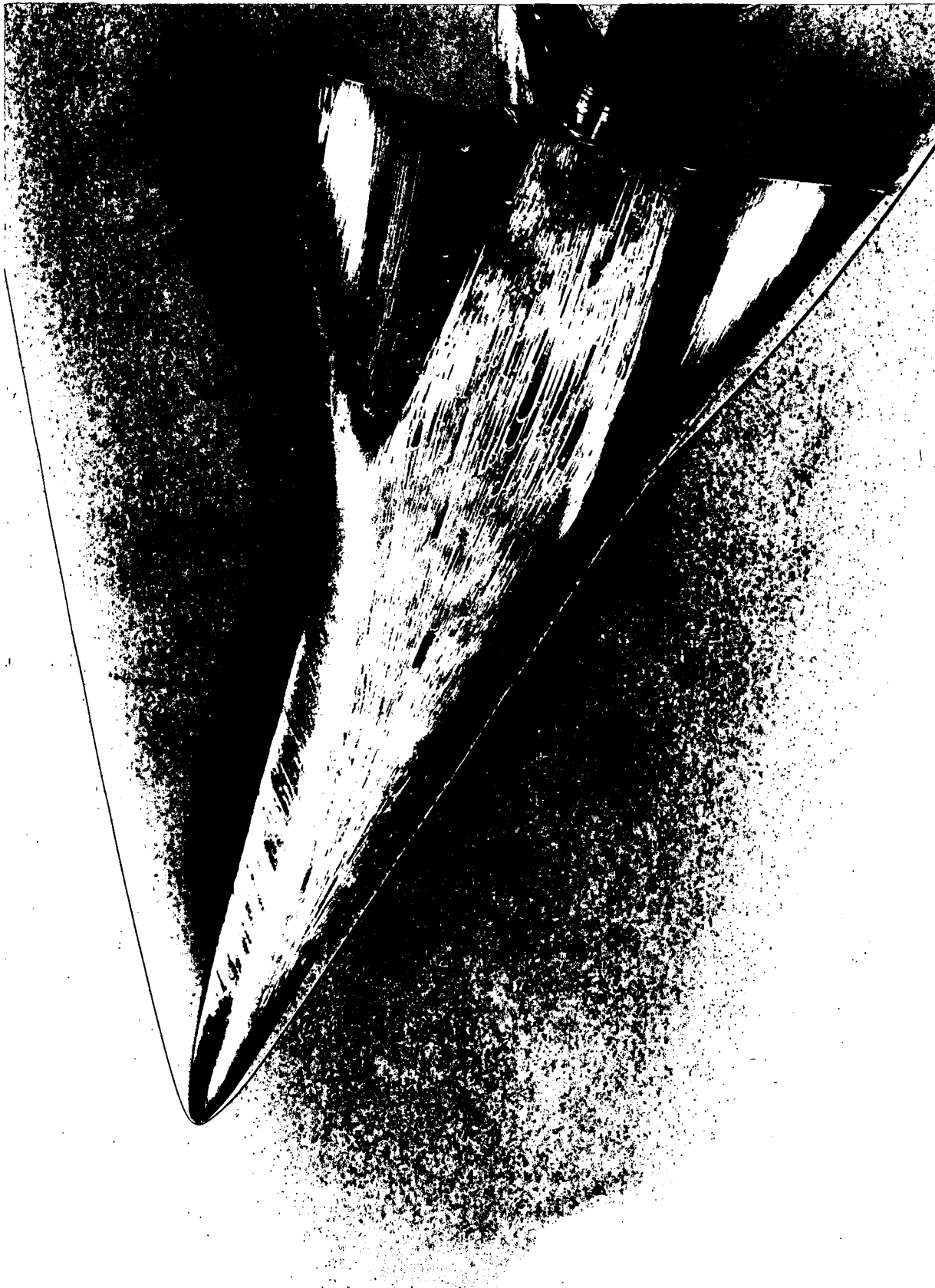
Figure 3.- Concluded.



(a) Plan view of the windward surface, $\phi = -90^\circ$.

Figure 4.- Flow over the model at an angle of attack of 30° .

$$\beta = 0^\circ, M_\infty = 7.4, Re_\infty = 9.0 \times 10^6.$$



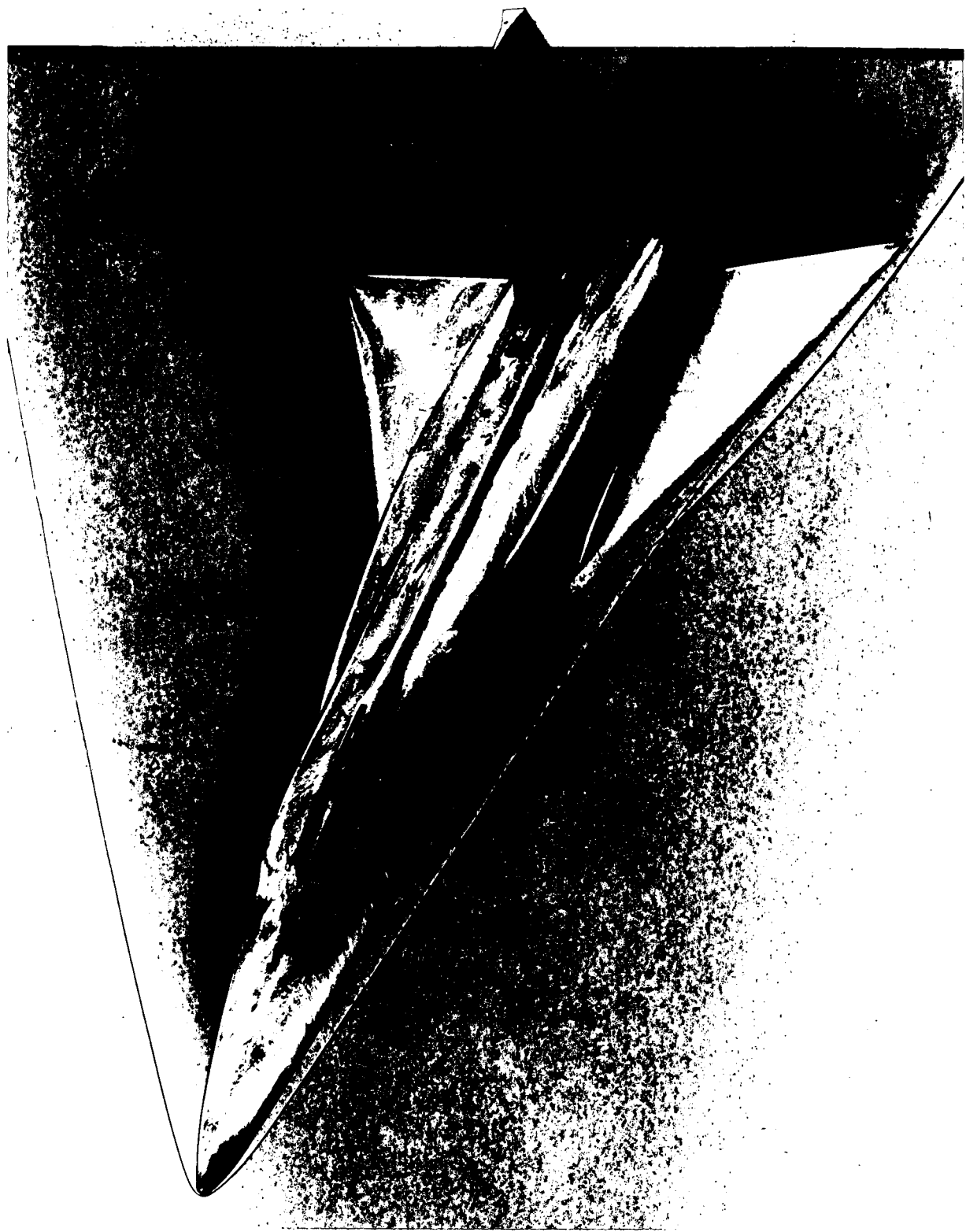
(b) Oblique view of the windward surface, $\phi = -45^\circ$.

Figure 4.- Continued.



(c) Side view, $\phi = 0^\circ$.

Figure 4.- Continued.



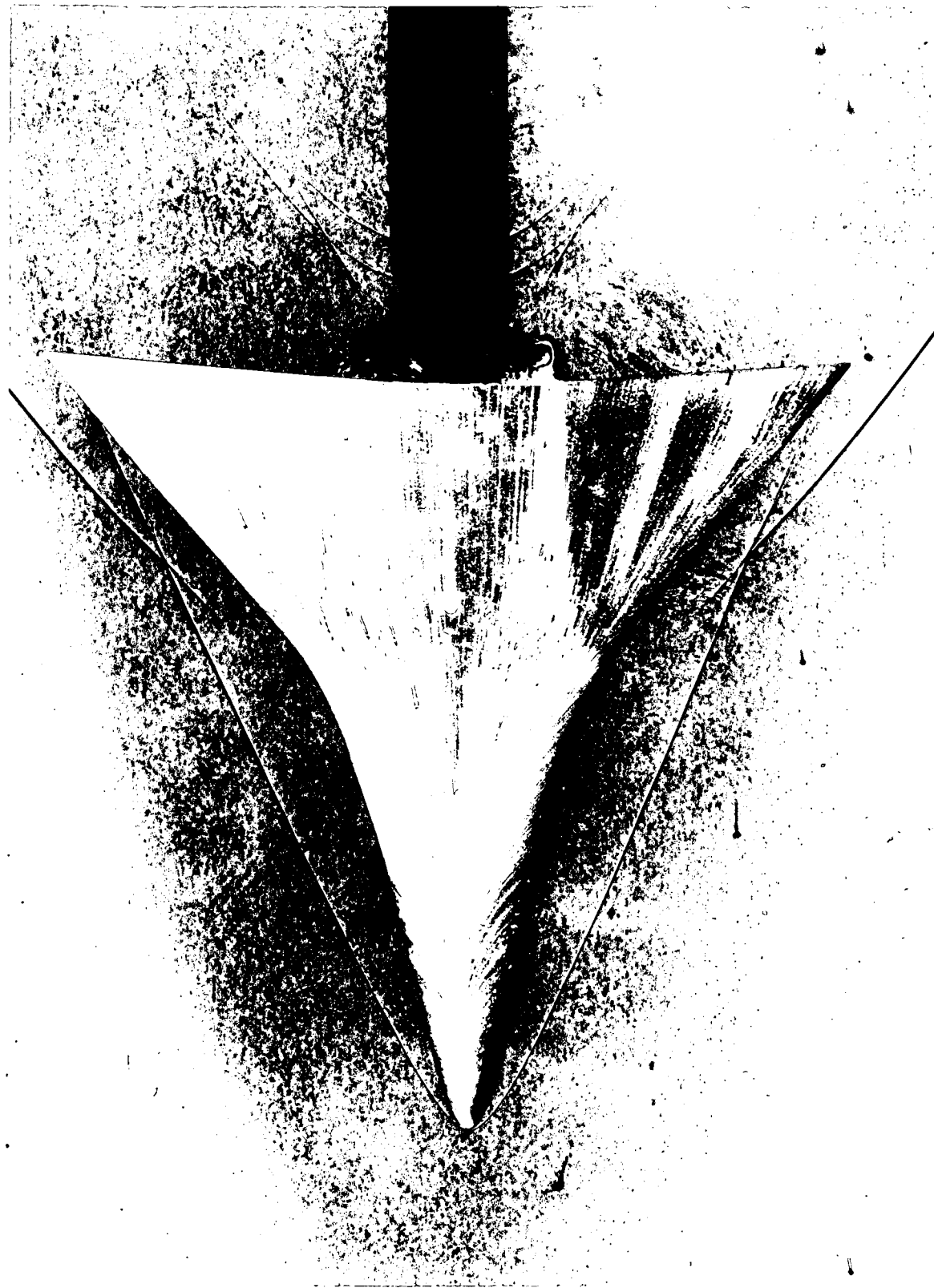
(d) Oblique view of the leeward surface, $\phi = 45^\circ$.

Figure 4.- Continued.



(e) Plan view of the leeward surface, $\phi = 90^\circ$.

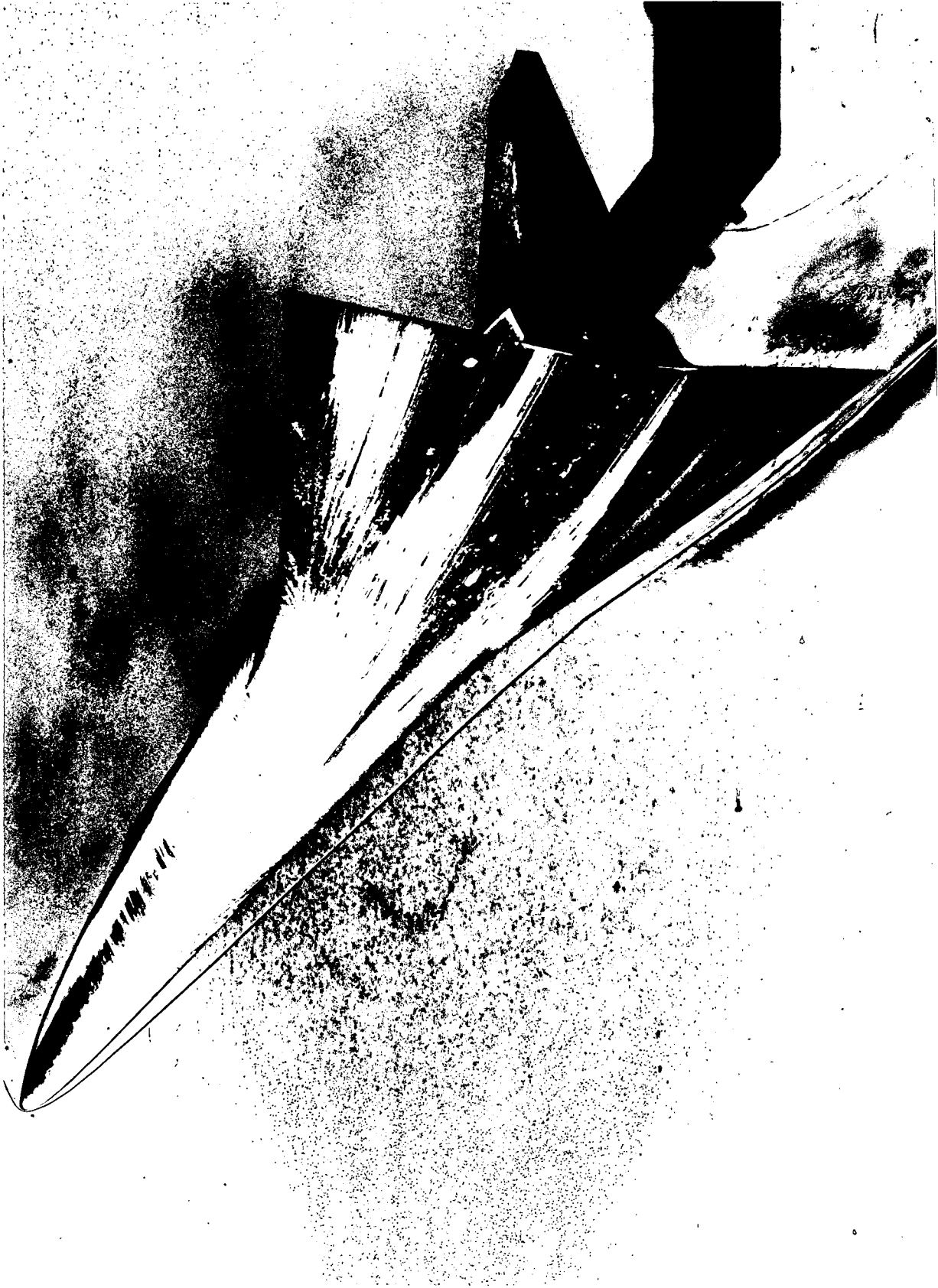
Figure 4.- Concluded.



(a) Plan view of the windward surface, $\phi = -90^\circ$.

Figure 5.- Flow over the model at an angle of attack of 45° .

$\beta = 0^\circ$, $M_\infty = 7.4$, $Re_\infty = 6.0 \times 10^6$.



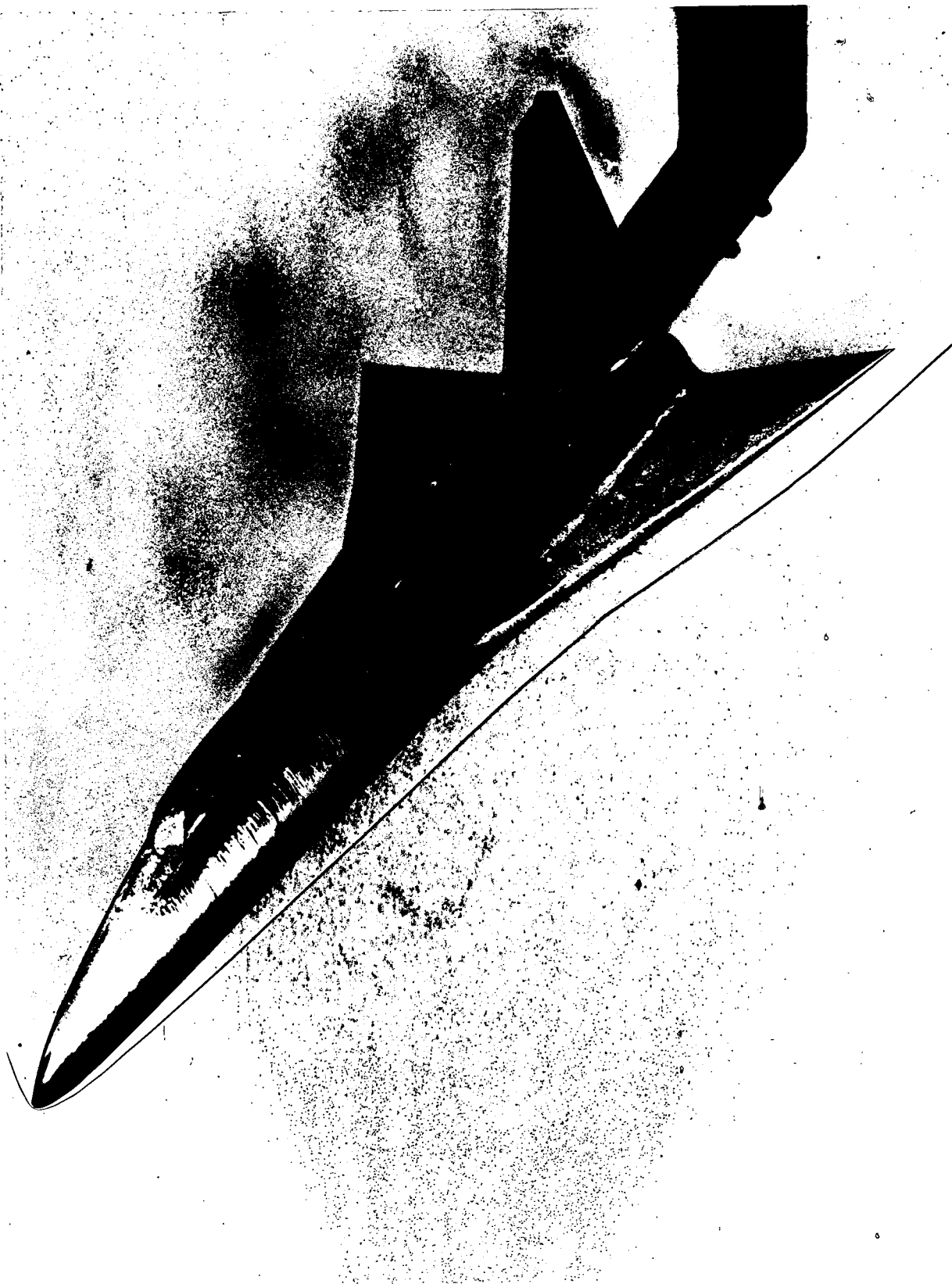
(b) Oblique view of the windward surface, $\phi = -45^\circ$.

Figure 5.- Continued.



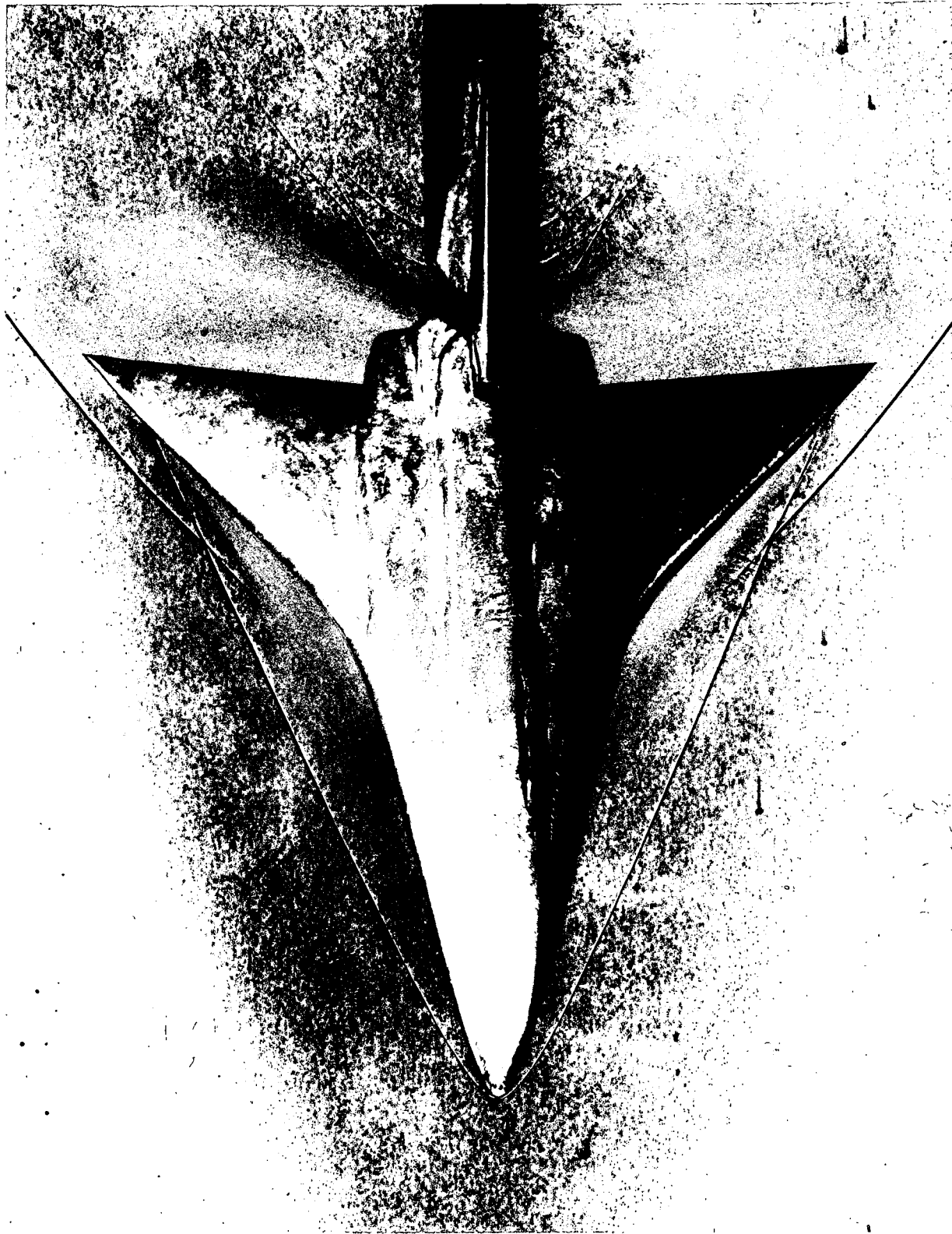
(c) Side view, $\phi = 0^\circ$.

Figure 5.- Continued.



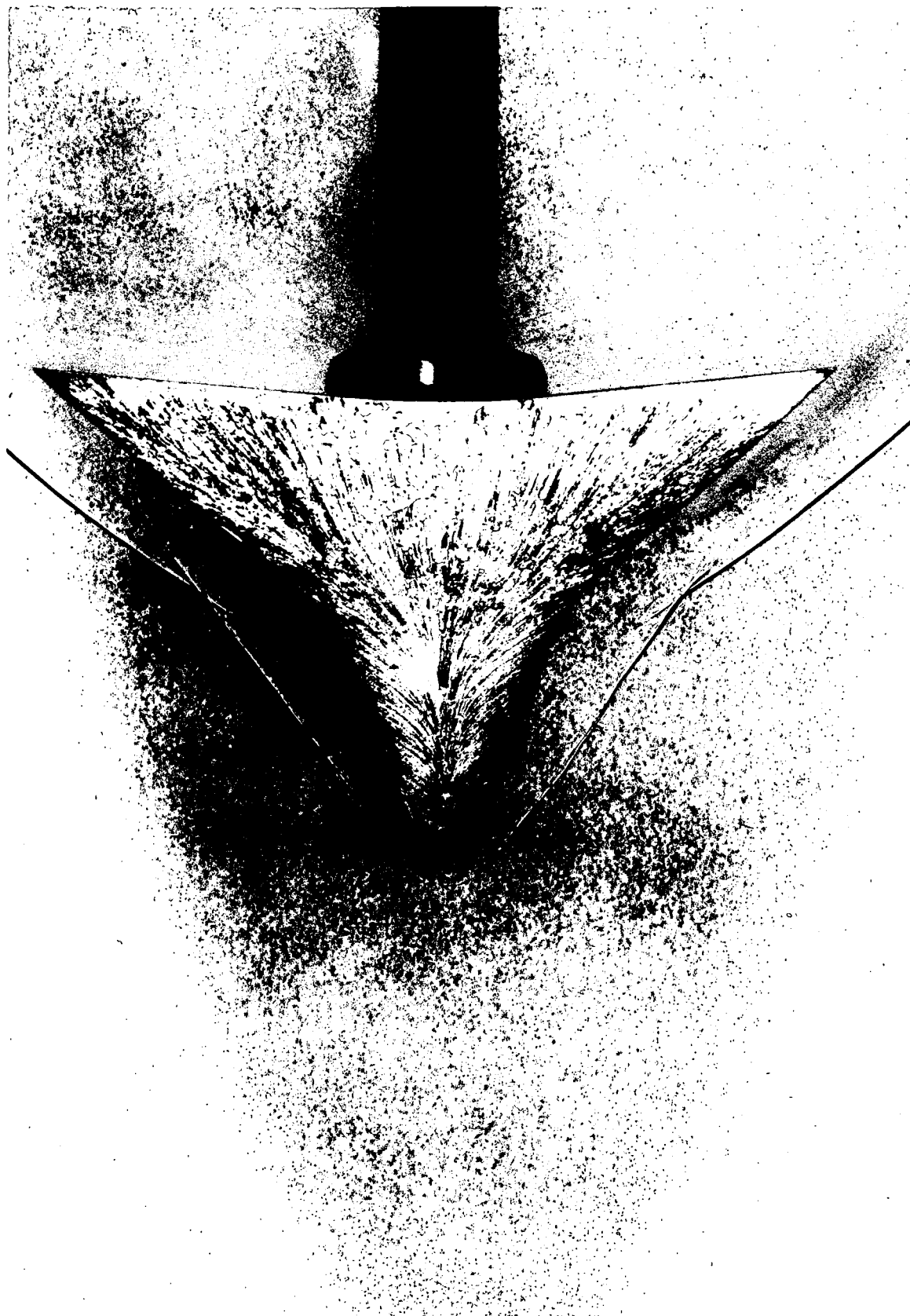
(d) Oblique view of the leeward surface, $\phi = 45^\circ$.

Figure 5.- Continued.



(e) Plan view of the leeward surface, $\phi = 90^\circ$.

Figure 5.- Concluded.



(a) Plan view of the windward surface, $\phi = -90^\circ$.

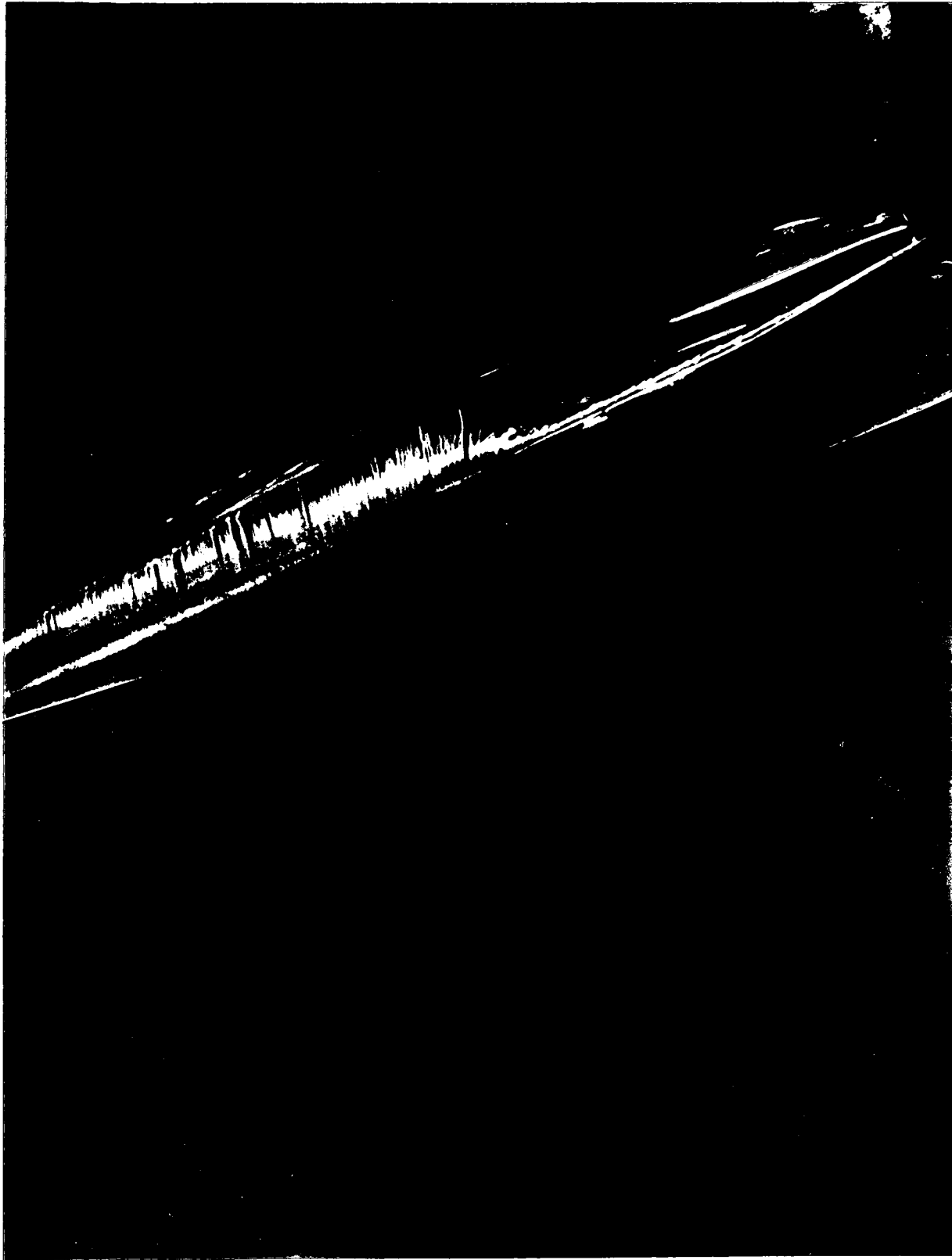
Figure 6.- Flow over the model of an angle of attack of 60°

$$\beta = 0^\circ, M_\infty = 7.4, Re_\infty = 6.0 \times 10^6.$$



(b) Oblique view of the windward surface, $\phi = -45^\circ$.

Figure 6.- Continued.



(c) Side view, $\phi = 0^\circ$.

Figure 6.- Continued.



(d) Oblique view of the leeward surface, $\phi = 45^\circ$.

Figure 6.- Continued.



(e) Plan view of the leeward surface, $\phi = 90^\circ$.

Figure 6.- Concluded.



(a) Plan view of the windward surface, $\phi = -90^\circ$.

Figure 7.- Flow over the model at an angle of sideslip of -10° .

$\alpha = 15^\circ$, $M_\infty = 7.4$, $Re_\infty = 9.0 \times 10^6$.



(b) Plan view of the leeward surface, $\phi = 90^\circ$.

Figure 7.- Concluded.